Acta Metallurgica Sinica (English Letters)
https://doi.org/10.1007/s40195-020-01088-y

Revealing a Transformation-Induced Plasticity (TRIP) Phenomenon in a Medium-Entropy Alloy

Ibrahim Ondicho[1,2,3] · Bernard Alunda[4] · Dicken Owino[5] · Luke Otieno[6] · Melody Chepkoech[7]

Received: 15 April 2020 / Revised: 23 May 2020

Abstract
A transformation-induced plasticity phenomenon in $Fe_{65}(CoCrMnNi)_{35}$ medium-entropy alloy was investigated. According to the X-ray diffraction patterns, the as-cast specimen contains a single-phase face-centered cubic (fcc), while low-temperature annealing at 500 °C and 600 °C leads to the introduction of a body-centered cubic (bcc) phase as a secondary phase. Further increment of the annealing temperature to above 700 °C eliminates the bcc phase, and the microstructure was found to contain a single-phase fcc. At 20% true strain, an fcc-to-bcc phase transformation is observed; whereas, at 28% true strain, an fcc-to-hcp phase transformation takes place as an additional deformation mechanism. This strain-induced phase transformation phenomenon leads to improved tensile properties of this alloy.

Keywords Phase transformation · X-ray diffraction · Mechanical behavior · Microstructure evolution · Multicomponent alloys

1 Introduction

Recent technological advances in aerospace, marine, automotive, chemical, and energy industries require materials with exceptional physical properties such as strength, toughness, and corrosion resistance, which can withstand extreme conditions [1–3]. However, the application of most conventional alloys is limited in such extreme environments. Therefore, an alternative approach to alloy design becomes inevitable. A recent breakthrough in the design and development of a new class of metallic materials called high-entropy alloys (HEAs) and medium-entropy alloys (MEAs) [4] has attracted a lot of scientific attention due to their outstanding properties in cryogenic [1], room temperature [5], high temperature [3], and corrosive conditions [6]. These alloys contain five or more principal elements, with each element having a concentration of between 5 and 35 at% in equiatomic or near equiatomic composition [7]. According to the existing principles of metallurgy, the microstructures of the HEAs would contain multiple phases. Nevertheless, they solidify as single-phase solid solutions such as face-centered cubic (fcc), body-centered cubic (bcc), and hexagonal-close packed (hcp) [8–10]. This phenomenon was initially attributed to the high intrinsic configurational entropy in these alloys, owing to the high number of principal elements involved [7]. Nonetheless, recent studies have highlighted that the high entropy effect is not the only parameter responsible for forming single-phase solid solutions [8].

Several strengthening mechanisms have been reported in HEAs and MEAs [11–14]. For instance, the widely studied equiatomic CoCrFeMnNi HEA and CoCrNi MEA have been reported to possess outstanding mechanical properties both

Available online at http://link.springer.com/journal/40195.

✉ Ibrahim Ondicho
ibrahim.ondicho@dkut.ac.ke

1 Department of Mechanical Engineering, Dedan Kimathi University of Technology, Private Bag-10143, Nyeri, Kenya

2 Materials, Design and Manufacturing (MADEMA) Group, Dedan Kimathi University of Technology, Private Bag-10143, Dedan Kimathi, Nyeri, Kenya

3 Department of Advanced Root Industry Engineering, Yuengnam University, Gyeongsan, South Korea

4 Department of Mining and Minerals Processing Engineering, Taita Taveta University, P.O. Box 635-80300, Voi, Kenya

5 Department of Mechanical Engineering, Inha University, Incheon, South Korea

6 School of Mechanical Engineering, Kyungpook National University, Daegu, South Korea

7 Department of Mechanical Engineering, Howard University, Washington, DC, USA

Published online: 18 June 2020

at room temperature and under cryogenic conditions [11, 15]. The excellent mechanical properties in these two alloy systems have been attributed to the solid solution hardening [12, 13], grain boundary strengthening [14], and mechanical twinning [11, 15]. A study of the deformation mechanisms of CoCrFeMnNi and CoCrNi having a similar grain size both at room temperature and cryogenic temperature (77 K) showed that during the early stages of plastic deformation slip is the dominant deformation mechanism. Moreover, nanotwinning becomes an additional deformation mechanism at higher plastic strains that delays necking, therefore improving the tensile properties of the above systems. However, it is noteworthy that the CoCrNi MEA shows a better stain hardening rate than the CoCrFeMnNi HEA due to its lower stacking fault energy (SFE) of approximately 22 ± 4 mJ m^{-2} which triggers profuse nanotwinning during plastic deformation.

Even though the aforementioned systems show remarkable mechanical properties, the cost of the constituent elements such as Ni and Co is high, which renders them economically unfeasible compared to the conventional steels [16]. A recent investigation by Ref. [17] highlighted the possibility of bridging the gap between the high-entropy concept and the high-alloyed steels by increasing the Fe content in the equiatomic CoCrFeMnNi HEA from 20 to 60 at%. In this study, it was shown that even though the yield stress (YS) decreases as the Fe content increases due to a reduced solid solution strengthening effect [12, 13], twinning-induced plasticity (TWIP) enhances the ultimate tensile strength (UTS) and the total elongation (TE), especially for the Fe60 alloy. This phenomenon is similar to that observed in TWIP steels, where the twin boundaries act as barriers to dislocation motion, thus impeding their motion, therefore improving their mechanical properties [18–20]. Several other reports about the mechanical properties and deformation mechanisms of HEAs and MEAs with a relatively higher content of Fe than that in the equiatomic CoCrFeMnNi HEA have been extensively studied. Yao et al. [21] studied the role of the configurational entropy in the phase formation and the tensile properties of $Fe_{40}Co_5Cr_2Mn_{27}Ni_{26}$ HEA. This alloy was reported to have a single-phase fcc. Therefore, it was concluded that the configurational entropy is not the sole determinant of phase formation in HEAs and that the compositional range of 5–35 at% is insufficient in defining the HEAs with a single-phase fcc. Additionally, they reported that the dominant deformation mechanism of this alloy was a slip. In a different study, the $Fe_{35}Mn_{45}Co_{10}Cr_{10}$ HEA was also reported to have a single-phase fcc in which the dislocation slip was the main deformation mechanism. However, due to a slight increase of the Fe content from 35 to 40 at% and a decrease of Mn content from 45 to 40 at% ($Fe_{40}Mn_{40}Co_{10}Cr_{10}$ alloy), a TWIP effect was activated. This phenomenon led to improved mechanical properties, especially at high strains where deformation is by both slip and nanotwinning. A recent study of $Fe_{60}Co_{15}Ni_{15}Cr_{10}$ MEA with an initial single-phase fcc reveals a transformation-induced plasticity (TRIP) phenomenon during plastic deformation. The parent fcc phase transforms to a bcc phase when deformed under cryogenic conditions, which causes an exceptional combination of strength and ductility [22]. The above attributes of utilizing phase metastability to achieve superior mechanical properties have also been widely explored and utilized in TRIP steels. The retained austenite, which is thermodynamically unstable, undergoes a phase transformation to form a bcc phase during deformation, hence exhibiting a good balance of strength and ductility [23, 24].

The above studies indicate that an alteration of the classic equiatomic composition, especially of the widely studied CoCrFeMnNi HEA, opens a wide compositional space to tune the mechanical properties of HEAs and MEAs by taking advantage of the innate strengthening mechanisms such as TWIP and TRIP. Therefore, increasing the Fe content in the CoCrFeMnNi system provides a possibility of harnessing the good properties of both HEAs and high-alloyed steels such as TRIP steels [18, 20]. In the present study, we reveal a TRIP phenomenon in a novel $Fe_{65}(CoCrMnNi)_{35}$ MEA (referred to as Fe65 in this study). The as-cast microstructure of Fe65 contains a dual- phase (fcc and bcc) upon solidification. On the other hand, when recrystallized, the phase fraction of fcc becomes the dominant phase with a small fraction of the retained bcc phase. Moreover, during plastic deformation, the fcc phase is transformed into α'-martensite (bcc) and ε-martensite (hcp), which improves the tensile strength and ductility of Fe65.

2 Experimental

This alloy was designed by increasing the Fe content to 65 at% while maintaining the equiatomic composition of the other four elements, with each having a concentration of 8.75 at%. The arc melting and tilt casting technique was used to fabricate the Fe65 MEA cylindrical ingot (Ø15 mm × 120 mm) under the pure Ar atmosphere. The starting materials consisted of pure elements with purity > 99.9 at%. All the elements were cleaned to remove dust and oxide layers before starting the casting process. An extra 1% of Mn was added to the crucible to compensate for the loss of Mn during the melting process due to its high evaporation rate. The as-cast ingot was homogenized at 1000 °C for 24 h to remove any possible segregation of elements during solidification. The as-homogenized ingot was cold-rolled into sheets of 1.5 mm thickness. The as-rolled specimens were recrystallized at a temperature range of 500–900 °C for 2 h using a salt bath. The X-ray diffraction

(XRD) technique was used for phase identification of both the as-cast and the recrystallized specimens using CuK_α radiation. To understand the phase evolution during deformation, electron backscatter diffraction (EBSD) measurements were carried out on specimens obtained from interrupted tensile tests at various true strains of the specimen heat-treated at 900 °C for 2 h. The specimen heat-treated at this condition was chosen based on the fact that it was found to contain a single-phase fcc. The EBSD data were analyzed using orientation imaging microscopy (OIM) collection software. The specimens used for XRD and EBSD analysis were mechanically polished by SiC paper with a surface grit of 2400 and then electro-polished using a 10% perchloric acid and 90% acetic acid solution. The tensile test was carried out using the dog-bone-shaped specimens having a gauge length of 10 mm and thickness of 1 mm at an engineering strain rate of 8×10^{-4} s^{-1}, and a digital image correlation technique (DIC) was used for precise measurement of strain.

3 Results

Figure 1a shows the phase diagram of the CoCrMnNi-Fe system. The details and further discussion about this phase diagram can be found in Ref. [17]. The dotted line (red) shows the approximate composition and possible phases of Fe65 at different annealing temperatures. For instance, the predicted phase for the specimen annealed at 900 °C is a single-phase fcc. A bcc phase is introduced as a second phase when the annealing temperature is reduced to approximately 600 °C. And finally, the sigma (σ) phase is introduced as a third phase at annealing temperatures below 500 °C. Figure 1b shows XRD patterns of as-cast and as-annealed specimens. A systematic heat treatment with a temperature range of 500–900 °C for 2 h was carried out to experimentally confirm whether the phases present are consistent with those predicted by the phase diagram. Interestingly, the as-cast specimen shows that Fe65 crystallizes into a fully single-phase fcc while those annealed at 500 °C and 600 °C for 2 h exhibit both fcc and bcc peaks. Finally, those specimens annealed at 700 °C, 800 °C, and 900 °C show fcc peaks only.

Figure 2a shows the engineering stress–strain curves for Fe60 and Fe65. Fe60 which is a single-phase fcc [17] was included in the present work to demonstrate the contributory effect of TRIP on the mechanical properties of Fe65. It was demonstrated by the previous work [17] that Fe60 did not undergo any phase transformation during plastic deformation and TWIP was confirmed to be the only additional strengthening mechanism. Figure 2b shows the YS, UTS, and TE as the composition changes from Fe60 to Fe65. First, it can be noted that a slight decrease in the YS from 158 to 155 MPa is observed when the Fe content is increased from 60 to 65 at%. This slight decrement indicates that a change of 5 at% of Fe has no significant effect on the YS. On the other hand, it is interesting that there is an increase in the UTS from 550 to 580 MPa. Additionally, an increase in strength is accompanied by a slight increase in TE by 2% when the Fe content is at 65 at%. The strain hardening rate of both Fe60 and Fe65 as a function of true strain is presented in Fig. 2c. Initially, the two curves show a similar tendency by decreasing gradually as the strain increases but a difference is observed at a true strain of about 15%. The strain hardening rate curve of Fe65 shows a slight up-turn indicating a possible activation of an additional deformation and strengthening mechanism such as TRIP phenomena.

Figure 3 shows the EBSD inverse pole figure (IPF), image quality (IQ), and phase maps of specimens from

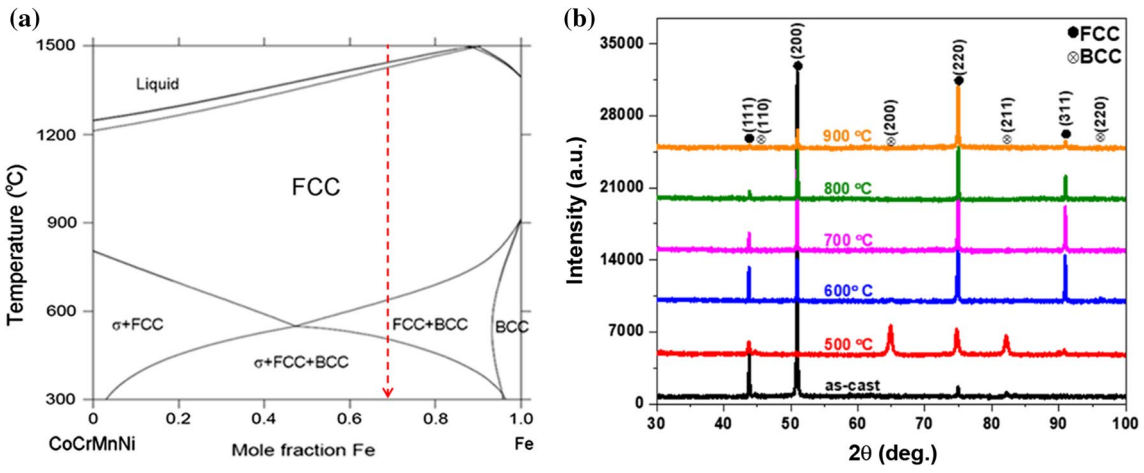

Fig. 1 **a** Phase diagram of CoCrMnNi-Fe system, **b** XRD patterns of as-cast and as-annealed specimens. The annealing was done at a range of temperatures (500–900 °C) for 2 h. (The phase diagram data were used with permission from Elsevier)

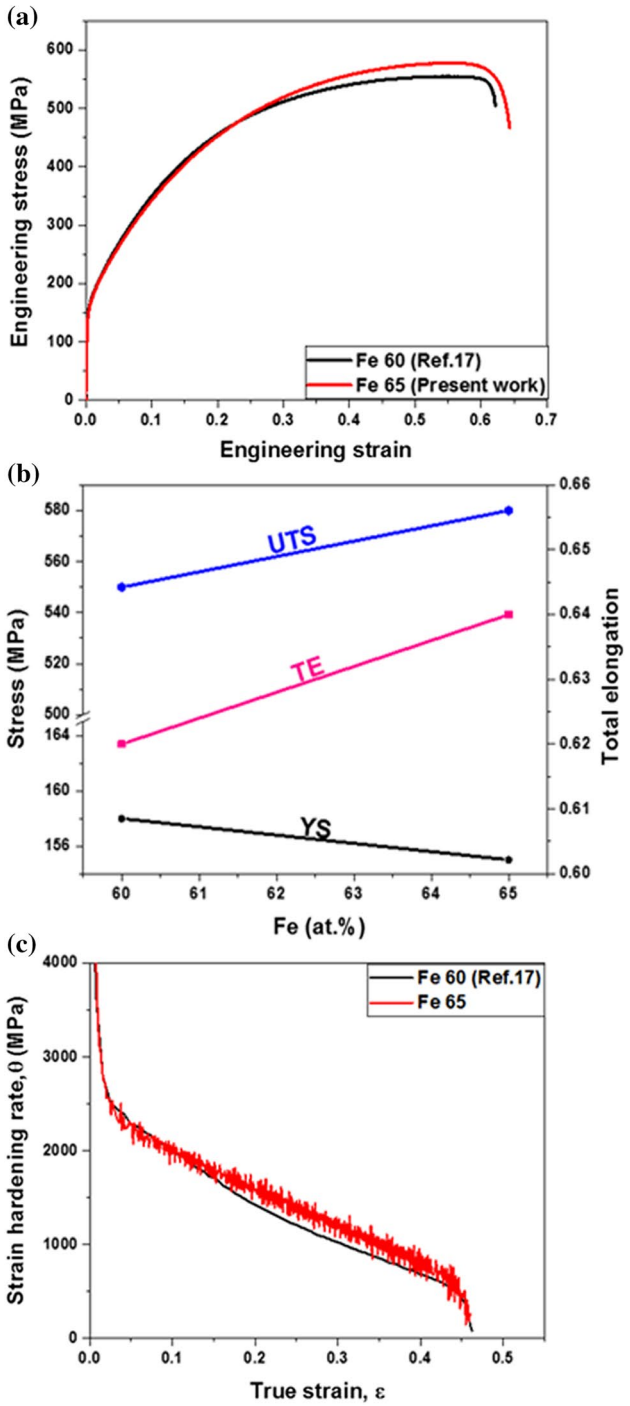

Fig. 2 **a** Engineering stress–strain curves of Fe60 and Fe65, **b** yield stress, ultimate tensile strength, and total elongation as a function of Fe, **c** strain hardening rate of both Fe60 and Fe65 as a function of strain

interrupted tensile tests. Figure 3a, b shows IPF images of specimens deformed up to 20% and 28% true strains, respectively, while (c) shows an IPF image from the necking region of the fractured specimen which has a local strain of 185.5%. The details on how to measure the local strain are reported in Ref. [17]. The IPF images show a homogenous microstructure with equiaxed grains. A random texture can also be observed. Additionally, deformation twins (DT) are observed in most parts of the microstructures especially in the grains with an orientation in the < 111 > direction. Moreover, the number of DT increases significantly at higher strains with the specimen from the necking region showing profuse DT formation. Phase quick maps of specimens interrupted at true strains of 20%, 28%, and local strain of 185.5% are presented in Fig. 3d-1, e, f. It is evident that these microstructures contain no precipitates. It is interesting to note that at the true strain of 20%, a phase transformation occurs where the metastable fcc phase transforms to a lath α'-martensite (bcc) phase which is nucleated in the DT and at the intersection of shear bands within an fcc grain. At this strain value, the ε-martensite (hcp) is not detected by the phase map. An inset in Fig. 3d-2 shows an enlarged nucleation site of the α'-martensite. Further plastic deformation up to a true strain value of 28% leads to nucleation of the ε-martensite phase in addition to the existing α'-martensite phase as shown in Fig. 3e. It is important to note that in some grains, the α'-martensite phase grows in the same nucleation site as that of the ε-martensite phase in the specimen deformed in up to a true strain value of 28%. Moreover, a specimen from the necking region (Fig. 3f) shows the presence of the three phases with a phase fraction of α'-martensite and ε-martensite being higher than that in Fig. 3e.

A clear quantitative analysis of phase evolution is presented in Fig. 4. Generally, the phase fraction of fcc decreases as the true strain increases while that of both the α'-martensite and ε-martensite increases proportionally. For instance, at 20% true strain, fcc is the dominant phase with a phase fraction of 98.5% while 1.5% is transformed to α'-martensite. This true strain value corresponds to a true stress value of 565 MPa. Further straining induces more phase transformation with a phase fraction of fcc slightly decreasing to 96.3% and that of α'-martensite remaining fairly constant at 1.4% while that of the newly formed ε-martensite is at 2.2%. This transformation occurs at 28% and 680 MPa true strain and true stress values, respectively. A phase fraction analysis of the specimen from the necking region (Fig. 3f) shows that a massive phase transformation from fcc to α'-martensite (bcc) and fcc to ε-martensite (hcp) takes place prior to fracture with corresponding phase fractions of 67.2% (fcc), 10.8% (bcc), and 21.7% (hcp).

Figure 5 presents an inset of EBSD phase maps of fcc, bcc, and hcp phases and their respective pole figures showing the orientation relationships (OR). The three phases were separated into individual phases and their pole figures were plotted separately in order to identify the type of OR that is present during the strain-induced phase transformation. Figure 5b–d

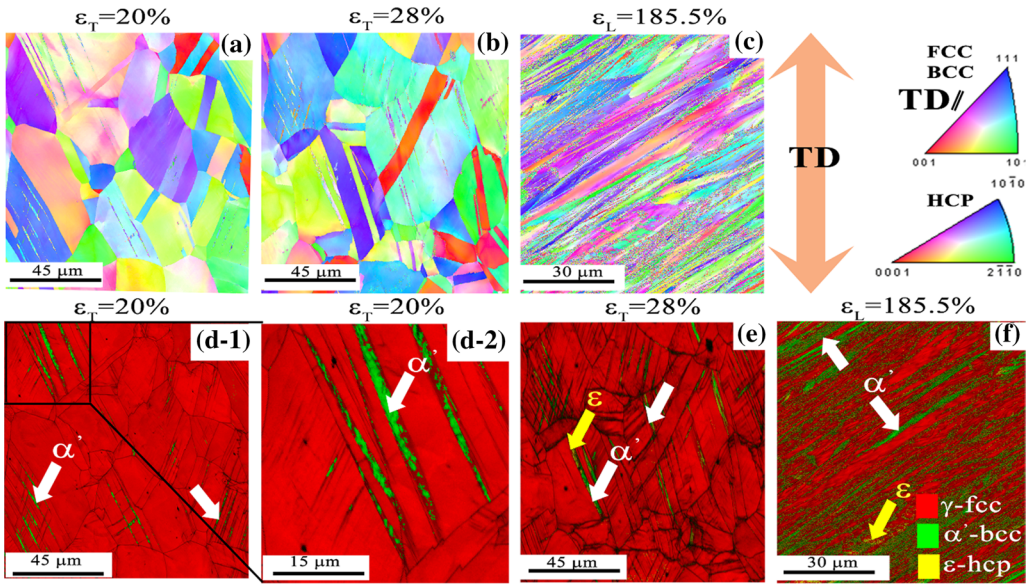

Fig. 3 EBSD inverse pole figure (IPF) and phase quick maps of specimens interrupted at various strains: **a, d-1, d-2** 20% true strain, **b, e** 28% true strain, **c, f** 185.5% local strain. TD refers to the tensile direction. ε_T denotes the true strain while ε_L denotes the local strain. The arrows in white color indicate nucleated α' martensite while those in yellow indicate ε-martensite. An inset is included in **d-2** to show the high resolution of nucleated α' martensite. The green and red colors in **(d-1, d-2, e, f)** indicate fcc and bcc phases, respectively

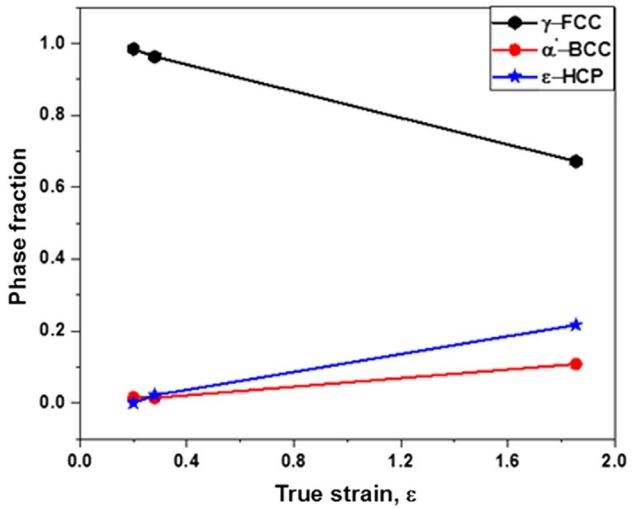

Fig. 4 Phase fraction evolution in Fe65 as a function of true strain during tensile deformation

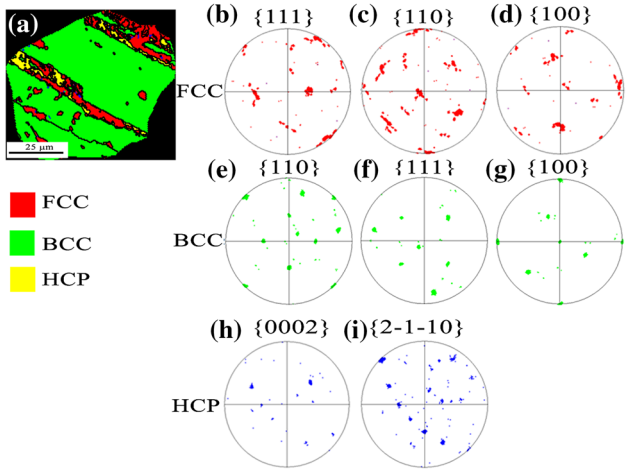

Fig. 5 **a** EBSD phase of fcc, bcc, and hcp after plastic deformation, **b–d** pole figures for fcc in {111}, {110}, and {100} planes, respectively, **e–g** pole figures for bcc phase in {110}, {111}, and {100} planes, **h**, **i** pole figures for hcp phase in {0002}, {2-1-10} planes. The red, green, and yellow colors represent fcc, bcc, and hcp phases, respectively

represents the pole figures of the fcc phase, (e)–(g) are the pole figures of the bcc phase, and (h) and (i) are the pole figures of the hcp phase.

4 Discussion

4.1 Phase Identification

Thermodynamic calculation and experimental results have been found to be consistent in the present study. It was

found that fcc is the thermodynamically stable phase of the as-cast specimen of the Fe65 alloy. Generally, annealing this alloy at temperatures between 500 and 600 °C introduces a secondary phase (bcc), while further increment of the annealing temperature to above 700 °C eliminates the bcc phase resulting in a microstructure with a fully single-phase fcc. It is noteworthy that there is a possibility of the phase fraction of fcc increasing while that of bcc decreasing as the annealing temperature is increased from 500 to 600 °C and then completely at temperatures above 700 °C. This is due to the fact that the (200) and (211) bcc peaks decrease in intensity as the annealing temperature is increased while at the same time the (200), (220), and (311) fcc peaks tend to increase. For further analysis of the mechanical properties of Fe65, specimen annealed at 900 °C for 2 h was chosen because it has single-phase fcc and a considerable coarse grains size. This was confirmed by a phase map analysis of the EBSD data of this particular specimen (not shown here) in addition to the XRD pattern shown in Fig. 1b, which showed that it is a single-phase fcc.

4.2 Mechanical Properties

The Fe65 MEA exhibits an interesting mixture of mechanical properties. The YS is observed to decrease slightly compared to that of Fe60 in spite of having some phase fraction of bcc. This indicates that the fraction of retained bcc phase is so small to have any substantial effect on the mechanical properties of Fe65. The slight decrease of the YS can be ascribed to the solid solution interaction effect in regards to the increased Fe content in the $Fe_x(CoCrMnNi)_{100-x}$ system [13]. At higher Fe content, as is the case of Fe65, the atomic size misfit is greatly decreased which leads to a significant decrease of the lattice distortion as compared to the equiatomic CoCrFeMnNi HEA. A less distorted crystal lattice will reduce the energy required for the movement of dislocations; therefore, Fe65 shows a slightly lower YS compared to that of Fe60. Conversely, the UTS and TE of Fe65 are higher than those of Fe60 as shown in Fig. 2a, b. It was reported that the main deformation mechanisms for Fe60 are slip and deformation twinning [17]. Therefore, the superior UTS and TE observed in Fe65 can be attributed to an additional strengthening mechanism during plastic deformation. This is further supported by its strain hardening behavior as shown in Fig. 2c. The strain hardening rate of both Fe60 and Fe65 initially decreases uniformly as the true strain increases. However, at a true strain value of approximately 15%, the strain hardening curve of Fe65 diverges from that of Fe60 indicating a possible starting point of an additional strengthening mechanism.

4.3 Phase Transformation

Shear bands in the form of ε-martensite (hcp), mechanical twins, and stacking fault bundles, which are formed during plastic deformation, can act as favorable nucleation sites for the strain-induced α'-martensite (bcc). These shear bands are associated with low intrinsic stacking fault energy [25, 26]. In the present study, α' martensite is nucleated inside DTs and at the intersection of shear bands after a plastic strain of 20% as shown in Fig. 3d-1. It is important to note that the nucleation process takes inside the fcc grains which are favorably oriented along the (111) plane during plastic deformation. At this stage of plastic strain, the ε-martensite is not nucleated and hence not detected by the phase map. According to Fig. 4, the formed α'-martensite corresponds to a 1.5% phase fraction and is responsible for the initial deviation of the strain hardening curve of Fe65 from that of Fe60. As mentioned above, ε-martensite plates can act as one of the nucleation sites of α'-martensite during plastic deformation [25]. This phenomenon was reported by Jo et al. [27] where they observed nucleation of bcc phases on the hcp phases in the $V_{10}Cr_{10}Fe_{45}Co_{30}Ni_5$ alloy system. A similar phenomenon is observed in the present study where α'-martensite (bcc) is nucleated inside DTs where the ε-martensite (hcp) has already been formed as shown in Fig. 3e. Nevertheless, it was observed that it is possible for the α'-martensite to be nucleated independently of ε-martensite, inside fcc grains which are oriented in the (111) plane where the nucleation of ε-martensite is greatly suppressed. This might be due to the ε-martensite not being thermodynamically stable to fcc phase or α'-martensite [26, 28]. This probably could be the reason why ε-martensite is absent in the early stages of plastic deformation as shown in Fig. 3d-1. The combined effect of phase transformation from fcc to α'-martensite, fcc to ε-martensite, and the pre-existing TWIP phenomenon is responsible for the superior UTS and TE in Fe65 MEA. Moreover, it is noteworthy that a high phase fraction of ε-martensite (21.7%) compared to that of α'-martensite (10.8%) as shown in Fig. 3f indicates that fcc to ε-martensite transformation is the dominant deformation mechanism prior to fracture.

4.4 Orientation Relationship

In the present study, a strained-induced phase transformation takes place where an fcc phase is transformed to bcc and hcp phases. It is reported that such martensitic transformations are accompanied by ORs between the parent phase and the product phase [29]. The most common ORs are Kurdjumow-Sachs (K-S) $\{111\}_{fcc} \parallel \{110\}_{bcc}$, $[011]_{fcc} \parallel [111]_{bcc}$ [30], Nishiyama-Wassermann (N-W) $\{111\}_{fcc} \parallel \{110\}_{bcc}$, $[11\text{-}2]_{fcc} \parallel [0\text{-}11]_{bcc}$ [31] for fcc-bcc relationship, and Shoji-Nishiyama $\{111\}_{fcc} \parallel \{0002\}_{hcp}$, $[011]_{fcc} \parallel [2\text{-}1\text{-}10]_{hcp}$ for

fcc-hcp relationship [32]. When planes and directions of the parent phase and the product phase match with each other, the interfacial energy is lowered and therefore a phase transformation is favored. A careful analysis of the pole figures presented in Fig. 5 reveals that K-S is the dominant OR of the martensitic transformation in Fe65 MEA. A superimposed image pole figure of $\{111\}_{fcc}$ and $\{110\}$ has several crystallographic matches between the two planes. Additionally, the pole figures in Fig. 5h, i show that the OR between the fcc and hcp show a Shoji-Nishiyama OR.

5 Conclusions

In the present study, a strained-induced phase transformation phenomenon in Fe65 MEA was successfully investigated. Therefore, our main findings can be summarized as follows:

1. Experimental phase analysis results were found to be consistent with those predicted by the thermodynamic calculation. According to the XRD pattern, the as-cast microstructure consists of a single-phase fcc, while those annealed at 500 °C and 600 °C for 2 h shows the presence of both fcc and bcc phases. However, increasing the annealing temperature to above 700 °C for 2 h eliminates the bcc phase, and a single-phase fcc microstructure is obtained.
2. The YS of Fe65 is lower than that of Fe60 due to its less distorted lattice crystal structure. However, its UTS and TE are improved due to the strain-induced phase transformation that occurs after a plastic strain of approximately 20%.
3. Lath α'-martensite (bcc) is nucleated in the DTs and at the intersection of shear bands mainly in the austenite (fcc) grains in the (111) orientation at 20% true strain. At 28% true strain, ε-martensite is also nucleated, and its phase fraction is higher than that of α'-martensite. The ε-martensite acts as an additional nucleation site for α'-martensite site since they can be observed to be nucleated alongside each other in some grains at a 28% true strain
4. At the initial stages of phase transformed, fcc-to-bcc phase transformation is favored as the additional deformation mechanism. Moreover, at higher true strains, fcc-to-hcp phase transformation is favored; hence, it is the dominant mechanism.
5. The analysis of the OR among the three phases, i.e., fcc, bcc, and hcp, reveals that a K-S OR exists between fcc and bcc and a Shoji-Nishiyama OR for fcc and hcp.

Acknowledgements This study was financially supported by the National Research Foundation of Korea (No. NRF-2015R1C1A1A01052856).

References

[1] B. Gludovatz, A. Hohenwarter, D. Catoor, E.H. Chang, E.P. George, R.O. Ritchie, Science **345**, 1153 (2014)
[2] S. Kalia, J. Low Temp. Phys. **158**, 934 (2010)
[3] T.K. Tsao, A.C. Yeh, C.M. Kuo, H. Murakami, Entropy **18**, 62 (2016)
[4] J.W. Yeh, JOM **65**, 1759 (2013)
[5] A.J. Zaddach, C. Niu, C.C. Koch, D.L. Irving, JOM **65**, 1780 (2013)
[6] Y. Qiu, M.A. Gibson, H.L. Fraser, N. Birbilis, Mater. Sci. Technol. **31**, 1235 (2015)
[7] J.W. Yeh, S.K. Chen, S.J. Lin, J.Y. Gan, T.S. Chin, T.T. Shun, C.H. Tsau, S.Y. Chang, Adv. Eng. Mater. **6**, 299 (2004)
[8] F. Otto, Y. Yang, H. Bei, E.P. George, Acta Mater. **61**, 2628 (2013)
[9] M. Feuerbacher, T. Lienig, C. Thomas, Scr. Mater. **152**, 40 (2018)
[10] A. Takeuchi, K. Amiya, T. Wada, K. Yubuta, W. Zhang, JOM **66**, 1984 (2014)
[11] G. Laplanche, A. Kostka, C. Reinhart, J. Hunfeld, G. Eggeler, E.P. George, Acta Mater. **128**, 292 (2017)
[12] I. Toda-Caraballo, P.E.J. Rivera-Díaz-del-Castillo, Acta Mater. **85**, 14 (2015)
[13] M.P. Agustianingrum, I. Ondicho, D. Jodi, N. Park, U. Lee, Mater. Sci. Eng. A **759**, 633 (2019)
[14] S.J. Sun, Y.Z. Tian, H.R. Lin, X.G. Dong, Y.H. Wang, Z.J. Zhang, Z.F. Zhang, Mater. Des. **133**, 122 (2017)
[15] G. Laplanche, A. Kostka, O.M. Horst, G. Eggeler, E.P. George, Acta Mater. **118**, 152 (2016)
[16] K.H. Lo, C.H. Shek, J.K.L. Lai, Mater. Sci. Eng. R **65**, 39 (2009)
[17] I. Ondicho, M. Choi, W.M. Choi, J.B. Jeon, H.R. Jafarian, B.J. Lee, S.I. Hong, N. Park, J. Alloys Compd. **785**, 320 (2019)
[18] B.C. De Cooman, O. Kwon, K.G. Chin, Mater. Sci. Technol. **28**, 513 (2012)
[19] I. Gutierrez-Urrutia, S. Zaefferer, D. Raabe, Scr. Mater. **61**, 737 (2009)
[20] O. Bouaziz, S. Allain, C.P. Scott, P. Cugy, D. Barbier, Curr. Opin. Solid State Mater. Sci. **15**, 141 (2011)
[21] M.J. Yao, K.G. Pradeep, C.C. Tasan, D. Raabe, Scr. Mater. **72–73**, 5 (2014)
[22] J.W. Bae, J.B. Seol, J. Moon, S.S. Sohn, M.J. Jang, H.Y. Um, B.J. Lee, H.S. Kim, Acta Mater. **161**, 388 (2018)
[23] S. Curtze, V.T. Kuokkala, M. Hokka, P. Peura, Mater. Sci. Eng. A **507**, 124 (2009)
[24] H. Ding, Z.Y. Tang, W. Li, M. Wang, D. Song, J. Iron. Steel Res. Int. **13**, 66 (2006)
[25] G.B. Olson, M. Cohen, Metall. Trans. A **6**, 791 (1975)
[26] G.B. Olson, M. Cohen, J. Less-Common Met. **28**, 107 (1972)
[27] Y.H. Jo, W.M. Choi, D.G. Kim, A. Zargaran, S.S. Sohn, H.S. Kim, B.J. Lee, N.J. Kim, S. Lee, Sci. Rep. **9**, 2948 (2019)
[28] J.F. Breedis, L. Kaufman, Metall. Trans. **2**, 2359 (1971)
[29] X.M. Zhang, E. Gautier, A. Simon, Acta Metall. **37**, 487 (1989)
[30] G. Kurdjumow, G. Sachs, Z. für Phys. **62**, 592 (1930)
[31] Z. Nishiyama, Sci. Rep. Tohoku Imp. Univ. **25**, 94 (1934)
[32] S.T. Pisarik, D.C. Van Aken, Metall. Mater. Trans. A **45**, 3173 (2014)